A scheme to account for arbitrary strains in kinetic Monte Carlo

Gopinath Subramanian,[1] Danny Perez,[1] Blas P. Uberuaga,[2] Carlos N. Tomé,[2] and Arthur F. Voter[1]

[1] *Theoretical Division, Los Alamos National Laboratory**

[2] *Materials Science & Technology Division, Los Alamos National Laboratory*

(Dated: February 25, 2013)

We present a method for efficiently recomputing rates in a kinetic Monte Carlo simulation when the existing rate catalog is modified by the presence of a strain field. We use the concept of the dipole tensor to estimate the changes in the kinetic barriers that comprise the catalog, thereby obviating the need for recomputing it from scratch. The underlying assumptions in the method are that linear elasticity is valid, and that the topology of the underlying potential energy surface (and consequently, the fundamental structure of the rate catalog) is not changed by the strain field. As a simple test case, we apply the method to a single vacancy in zirconium diffusing in the strain field of a dislocation, and discuss the consequences of the assumptions on simulating more complex materials.

I. INTRODUCTION

The kinetic Monte Carlo (kMC) method[1,2] is a widely used technique to simulate the long time evolution of many systems of practical interest. It has been used to study a variety of phenomena such as surface and bulk diffusion[3,4], microbial ecologies[5], cascade annealing[6,7], and thin film growth[8,9]. A number of enhancements over the last few decades have resulted in improved methods such as absorbing Markov chains[10], adaptive kMC[11], object kMC[12], and accelerated superbasin kMC[13]. In the kMC method, a system is advanced from one minimum energy configuration to the next by knowing, or computing on the fly, the different escape pathways from a minimum, and the escape rates for each of those pathways (the list of escape pathways and associated escape rates is commonly referred to as a rate catalog). The escape rates, in turn, are usually given within the purview of transition state theory (TST), and are a function of the system temperature, energy barrier, and a rate prefactor that is often computed using Vineyard's expression[14] for harmonic TST rates, or simply assumed to be a standard value, typically about 10^{12} s^{-1}.

In many applications, one is particularly interested in how a system of atoms evolves in the presence of strain, which can dramatically alter the atomic scale events and overall system evolution. For example, in thin film growth, lattice mismatches lead to strains and eventually different film morphologies[15]. The effect of externally applied strain has also been shown to enhance the rate of material dissolution and the formation of etch pits[16], modify the diffusion rate of impurities in nanowires[17], and *qualitatively* change the behavior of both atom detachment from a step, and dimer dissociation of Ag on an Ag(100) surface[18]. Another source of strain that is commonly discounted in kMC simulations is thermal expansion: the rate catalog is often based on defect properties calculated in a constant volume ensemble, using the lattice parameter computed at $T = 0$ K[19,20]. This type of calculation does not account for the thermal eigenstrain, which depending on the coefficient of thermal expansion of the material, can significantly change the rate catalog. Internal strains can also have an important influence on the phenomena of irradiation creep and irradiation growth[21] where the unit process dictating the macroscopic strain rate of the material is the absorption of point defects and defect clusters by sinks such as dislocations and grain boundaries. Different types of sinks produce inherently different strain fields, modify point defect mobility in their vicinity, and consequently absorb point defects at different rates, ultimately leading to modified macroscopic strain rates.

The strain induced change in the rate catalog is automatically accounted for in an on the fly kMC, but recomputing the rate catalog at every step can be computationally expensive: even the most efficient implementation must perform a finite number of force evaluations, dramatically increasing the computational cost when compared with a conventional kMC simulation. Other more approximate methods of accounting for this strain induced change include explicitly precomputing the rate catalog as a function of strain[22–25], using artificial neural networks to account for long range interactions[26], or using system specific methods of estimating the energy barrier change as a function of strain[27,28].

In this paper, a scheme to efficiently account for arbitrary strain fields in kMC simulations is presented. This scheme is not designed to explore the potential energy landscape of a system (which itself can be a formidable challenge and is an issue for all kMC simulations), but to incorporate the effects of strain into an existing kMC rate catalog. In this scheme, the strain induced changes to the energy barriers are computed using the double dot product (or scalar product) of the dipole tensor with the strain tensor. The strain induced changes to the prefactors may be ignored, because for point defects and defect clusters, the change in energy barriers has the most significant effect on the net transition rate (except at very high temperatures), and the changes in the prefactors themselves are small (e.g., Matsunaka and Shibutani[25] found $\approx 6\%$ change in the prefactors for a 2% strain). The range of applicability and limitations of the scheme are also discussed. As an example system, the mobility of a single vacancy in α zirconium is examined. The interatomic potential used is the third embedded atom method (EAM) potential by Mendelev and Ackland[29]. Preliminary results obtained on single self interstitial atoms (SIAs) are also presented. For all simulations, the X, Y, and Z axes of the simulation cell were aligned along the $[2\bar{1}\bar{1}0]$, $[01\bar{1}0]$, and $[0001]$ crystallographic directions, respectively.

II. METHODS

A. Discovering and characterizing transitions

The initial (or reference) configuration of a vacancy was created by removing a single atom from a perfect crystal and performing an energy minimization. The different types of transitions that the vacancy could undergo were determined by running molecular dynamics (MD) at a temperature of 1100 K from the reference configuration. During the MD run, the "hot" configuration was periodically quenched. If any atom had moved more than 1 Å from the reference configuration, a transition was said to have occurred. If there was no transition, MD was simply continued. If a transition had occurred, it was characterized, the reference configuration was restored, and MD was started anew. All transitions were characterized by recording the displacement vector d**r** associated with them, and obtaining the

energy and structure of the saddle point using the climbing image nudged elastic band (CI-NEB)[30–32] method. For our example defect of a single vacancy, the only transitions that were relevant were the in plane and out of plane transitions, as expected. However, for a more complex defect, for which the transitions cannot be easily guessed, this basin constrained MD procedure becomes important.

B.   Dipole tensor computation

As mentioned above, the energetics of different minima and the transitions between them are affected by strain fields. The change in energy of a minimum, or a saddle point associated with a transition, due to a strain $\boldsymbol{\varepsilon}$ is given to first order by[33–35]

$$\Delta E = -G_{ij}\varepsilon_{ij} \tag{1}$$

where $\mathbf{G}$ is a second order tensor called the dipole tensor, and the Einstein summation convention has been used. It must be stressed that in this definition, the value of ΔE is the change in energy of the defect alone, and does not include contributions from bulk elastic strain energy. Thus, in the procedure outlined below, the elastic contribution is subtracted out. In other words, the value of ΔE is computed as the difference in formation energies between strained and unstrained environments. Two prominent methods of computing the dipole tensor are available in the literature, namely, the Kanzaki Hardy forces method[36,37], and Gillan's strain derivative relation[38,39]. The latter method is used in this paper because (a) it has been shown to be the more accurate of the two[38], and (b) it is applicable to complex defects (such as interstitial clusters), a situation where the Kanzaki Hardy forces method might not be easily applicable due to the difficulty in unambiguously deciding which atoms are part of the defect, and which atoms are part of the environment. In Gillan's strain derivative relation, the derivative of ΔE with respect to each component of strain is extracted numerically from equation 1. The procedure adopted is as follows:

In order to compute the ij^{th} component of the dipole tensor of a minimum structure (in the present test case, a vacancy), the starting point was a relaxed (minimum energy) configuration. The simulation box was first subjected to a small, far field strain component $\Delta\varepsilon_{ij} > 0$, with all other strain components set to zero. The boundary atoms were held fixed while the rest of the structure was relaxed. The change in energy between the two relaxed structures was measured, and denoted as $\Delta(\Delta E)^+$.

In order to compute the ij^{th} component of the dipole tensor of the saddle point, the chain of states from the NEB calculation was taken to be the starting point. All images on the chain were subjected to a small, far field strain component $\Delta\varepsilon_{ij} > 0$. The boundary atoms of all images on the chain were held fixed, and the NEB procedure was repeated to obtain a new saddle corresponding to the strained chain of states. The change in energy between the strained and unstrained saddles was measured, and denoted as $\Delta(\Delta E)^+$.

For both the minimum and the saddle point, the energy change measurement was repeated with a strain $-\Delta\varepsilon_{ij}$, and the change in energy obtained in this case is denoted as $\Delta(\Delta E)^-$. The value of G_{ij}, for both the minimum and the saddle point, is then given as

$$G_{ij} = -\frac{\Delta(\Delta E)^+ - \Delta(\Delta E)^-}{2\Delta\varepsilon_{ij}} \tag{2}$$

The procedure was repeated for all ij components of the dipole tensor, with a value of $\Delta\varepsilon_{ij} = 10^{-4}$. Note that this method of computing $\mathbf{G}$ assumes that the change in energy is linear with strain. It is conceivable that higher order terms might need to be included in equation 1, depending of the type of the defect, and particularly in high strain situations.

C.   Incorporating the effects of strain in an object kMC

The list of minima, transitions associated with each minimum, and displacement vectors d$\mathbf{r}$ associated with each transition form the basic kMC catalog (in the present example case there is only one minimum, namely a single vacancy), and the full kMC catalog included all possible degeneracies of the minimum due to crystal symmetry, and accounted for symmetry transformations of the various displacement vectors d$\mathbf{r}$ and dipole tensors $\mathbf{G}$. This full rate catalog was then used in an object kMC simulation[12] where multiple objects, each with their own rate catalog, are present in the simulation. Given this rate catalog, the rest of the kMC simulation proceeds much as in standard kMC[2], but with important differences in the calculation of energy barriers. For clarity, the entire procedure is outlined below:

1. Let the total number of objects be denoted by $N_{objects}$, the number of possible transitions associated with the ith object be denoted by $N^{(i)}_{transitions}$, and the total number of possible transitions over all objects be denoted by N, which is given by $N = \sum_i N^{(i)}_{transitions}$

2. Initialize: The objects (in the present example case, all objects are vacancies) are placed in their initial minimum, and position $\mathbf{R}^{(i)} = \mathbf{R}^{(i)}_0$, where the superscript i refers to the object number.

3. Begin loop over all objects $i \in [1, N_{objects}]$

4. Begin loop over all transitions $j \in [1, N^{(i)}_{transitions}]$ that are associated with object i

5. Recalculate energy barrier: Given a strain field $\varepsilon(\mathbf{R})$ (either analytically or in the form of a table), the energy barrier is recomputed as

$$E_a^{(i,j)} = (E + \Delta E)^{(i,j)}_{saddle} - (E + \Delta E)^{(i)}_{minimum} \tag{3}$$

where E refers to the unstrained energy, and the values of ΔE are given by equation 1. The subscripts *saddle* and *minimum* refer to quantities pertaining to the saddle point for that transition, and the minimum energy configuration of the object, respectively. For the minimum, strain is evaluated at the position of the defect as $\varepsilon(\mathbf{R}^{(i)})$. For the saddle, strain is evaluated at the halfway point of the transition as $\varepsilon(\mathbf{R}^{(i)} + 0.5 \times \mathrm{d}\mathbf{r}^{(i,j)})$ (Note that in general, the saddle point need not be at the midpoint of the transition).

6. Recalculate rate: Having recomputed the energy barriers for each transition, the rate is recalculated as

$$k^{(i,j)} = k_0^{(i,j)} \exp\left(\frac{-E_a^{(i,j)}}{k_B T}\right) \tag{4}$$

where $k_0^{(i,j)}$ is the prefactor computed from the Vineyard expression[14]. The strain induced change in the prefactor has been ignored, because a change in $k_0^{(i,j)}$ has relatively little effect on $k^{(i,j)}$ when compared with the change in $E_a^{(i,j)}$, except at high temperatures.

7. Create a one to one mapping between every pair of indices (i, j), and a single index m.

8. End loops over j and i.

9. Recompute the partial sums over every transition $m \in [1, N]$ as

$$K^{(m)} = \sum_{n=1}^{n=m} k^{(n)} \tag{5}$$

10. Generate a uniformly distributed random number $u \in (0, 1)$, and choose the transition m for which $K^{(m-1)} < uK^{(N)} \le K^{(m)}$.

11. Advance the simulation clock by a time

$$\Delta t = \frac{1}{K^{(N)}} \ln\left(\frac{1}{v}\right) \tag{6}$$

where v is another uniformly distributed random number $v \in (0, 1)$

12. Displace the chosen object by the displacement vector associated with the chosen transition, and place it in its new position $\mathbf{R}^{(i)}(t + \Delta t) = \mathbf{R}^{(i)}(t) + \mathrm{d}\mathbf{r}^{(i,j)}$

13. Go back to step 3 and repeat

TABLE I. List of dipole tensor values **G** for the minimum energy configuration of the vacancy, and the saddle points for the two basic transitions discussed in the text. Also given are the displacement values associated with each transition. This table does not include degeneracies due to crystal symmetry. Distances are in Å, while energy and G_{ij} values are in eV. The X, Y, and Z axes of the simulation cell were aligned along the $[2\bar{1}\bar{1}0]$, $[01\bar{1}0]$, and $[0001]$ crystallographic directions, respectively.

				G_{11}	G_{22}	G_{33}	G_{23}	G_{13}	G_{12}
Vacancy minimum (V)				-5.20	-5.20	-5.81	0.00	0.00	0.00
	Energy Barrier	Displacement dx dy dz		G_{11}	G_{22}	G_{33}	G_{23}	G_{13}	G_{12}
Out of plane transition	0.7227	0.00 1.87 2.58		-8.36	-3.27	-7.01	-4.08	0.00	0.00
In plane transition	0.6535	3.23 0.00 0.00		-9.32	-3.33	-6.18	0.00	0.00	0.42

Note that in the procedure described above, the effect of strain is not applied to the displacement vector d**r** during the kMC run. This ensures that for any transition, the saddle point energy is the same in both the forward and backward directions, thereby satisfying detailed balance. As a consequence, the spatial trajectory of an object as obtained from the kMC simulations does not contain the effect of strain, and in order to obtain the actual trajectory of the object, the strain field should be applied *a posteriori*, and can be important in computing quantities such as diffusivity. However, the time scale between events does indeed account for strain, and any temporal measure of the trajectory is accurate.

Certain steps in the procedure outlined above can be eliminated if deemed unnecessary, e.g., if an object is not moved in a kMC step, and the strain tensor for the object and its transitions are unchanged, there is no need to recompute its rate catalog. Furthermore, reactions between objects can be defined, as done by Domain et al.[12], and the strain field produced by the objects themselves can be incorporated into the simulation. These complexities are beyond the scope of this paper, and will be addressed in future publications.

III. RESULTS AND DISCUSSION

A. Comparison of measured and predicted energies

The single vacancy was observed to be capable of two types of migration: one out of the basal plane and another in the basal plane. Out of plane migration was a simple vacancy hop, with a barrier of 0.723 eV. In plane migration was slightly more complex. A vacancy executing an in plane hop was seen to exhibit a second type of structure in between the hop, which we will call a split vacancy. As shown in Appendix A, the split vacancy minimum can be ignored as it is very shallow (0.01 eV), and the majority of transitions from a normal vacancy to a split vacancy, as observed in MD simulations, continue forward to move the vacancy to the next lattice site (i.e. the transmission coefficient is close to unity). Furthermore, the lifetime of the split vacancy is negligibly small. Consequently, the in plane migration of a vacancy, through the split vacancy structure, was considered to be a single transition with a barrier of 0.654 eV. Thus, for the purposes of this study, a vacancy was considered to have only one type of structure, and two types of transitions out of this structure. The dipole tensor values of the vacancy and its transitions are given in table I. There are in fact two types of vacancies, depending on whether the vacant site belongs to the A or B layer of the HCP lattice, and a total of 12 possible transitions each vacancy type can undergo. The full kMC catalog is obtained by performing symmetry operations on the vacancy and its basic transitions. These symmetry operations and the additional complexity posed by the split vacancy (viz. the asymmetry of the two saddle points associated with the in plane hop) are outlined in Appendix B.

The dipole tensor values were validated by comparing the energetics obtained from equation 1 with explicit atomistic calculations of the vacancy in various strain fields. In particular, a vacancy configuration was subjected to a far field strain, minimized, and the energy compared with a configuration with zero strain. For the saddle, each image from the chain of states of the NEB calculation was subjected to a far field strain, the saddle reconverged, the new saddle point energy measured, and the new energy barrier computed. The results of the comparison are shown in Fig. 1 for the minimum, and Fig. 2 for both transitions. The range of strain used was $\varepsilon_{ij} \in [-0.02 : 0.02]$.

The agreement between the measured energy values and the dipole tensor predictions are in good agreement for small strains (about 1%), and for all the different strain components. For larger strains, however, deviations from the predicted values are observed. Most notable of these is the energy barrier for an out of plane hop (open circles in Fig. 2 (b)), which deviates by about 0.02 eV for a 2% tensile strain along the X direction. This deviation, while larger than the others, is still less than 3% from the predicted value. For a compressive strain in the same direction, the deviation is smaller. These results show that for single strains, changes to the energy barriers can be computed
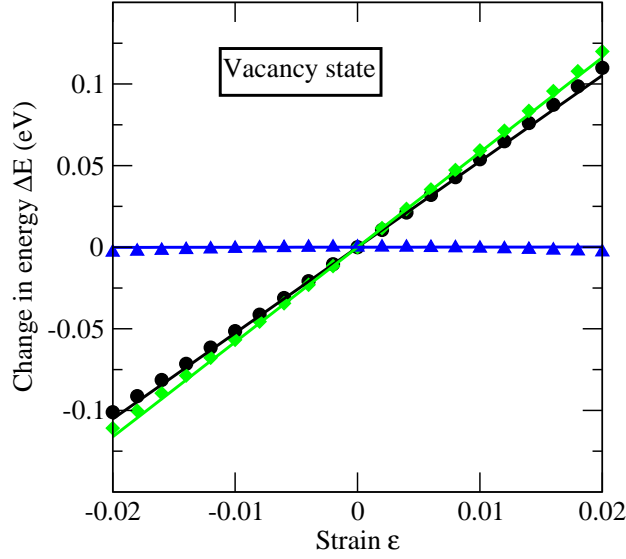
FIG. 1. (Color online) Change in energy of a vacancy as a function of strain for different types of strain. Symbols are data obtained from molecular statics, and lines are predictions made using the dipole tensor and equation 1. The different strains are ε_{11} ($\bullet$), ε_{33} ($\blacklozenge$), ε_{23} ($\blacktriangle$). ε_{22} is not shown, as its results are identical to the results of ε_{11}. ε_{12} and ε_{13} are not shown, as their results are identical to the results of ε_{23}.
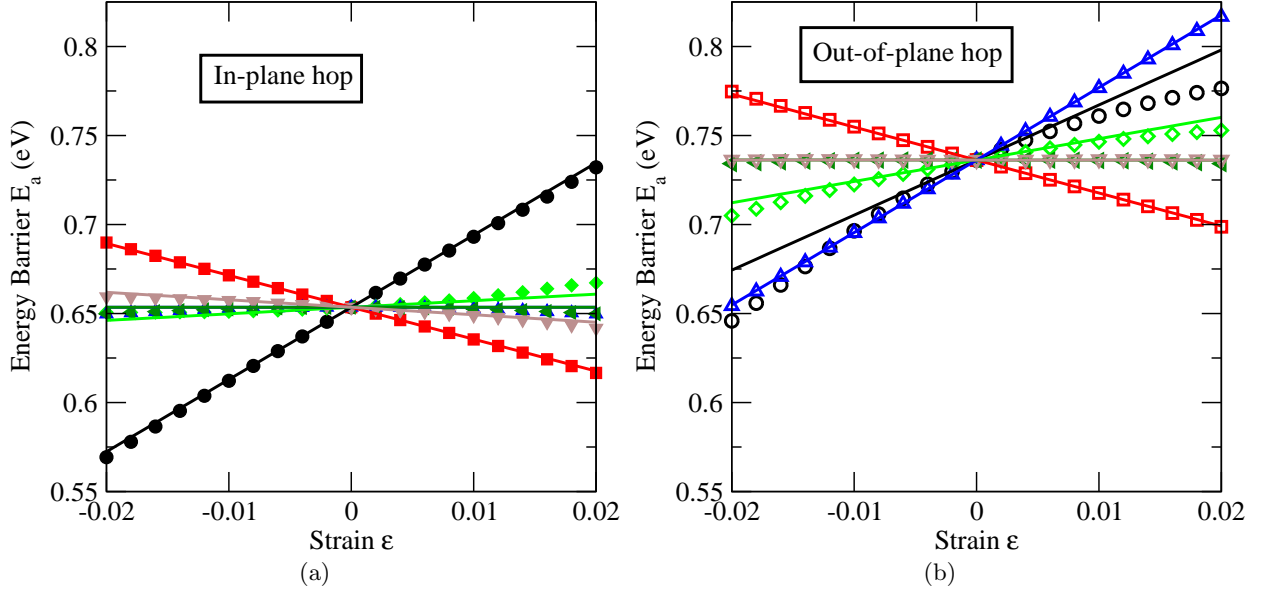
FIG. 2. (Color online) Energy barriers as a function of strain. Symbols are data obtained from the CI-NEB, while lines are predictions made using the dipole tensor for (a) in plane vacancy hop (filled symbols), and (b) out of plane vacancy hop (open symbols). The different strains are ε_{11} ($\bullet$), ε_{22} ($\blacksquare$), ε_{33} ($\blacklozenge$), ε_{23} ($\blacktriangle$), ε_{13} ($\blacktriangleleft$), ε_{12} ($\blacktriangledown$).

accurately using the dipole tensor relationship in equation 1. In the next subsection, the effect of more complex strain fields is examined.

B. Vacancy energetics in the vicinity of an edge dislocation

Following Hayward et al.[40], who performed a similar treatment for BCC iron, a comparison between the energetics of a vacancy in the vicinity of an edge dislocation as predicted using the dipole tensor, and directly measured from
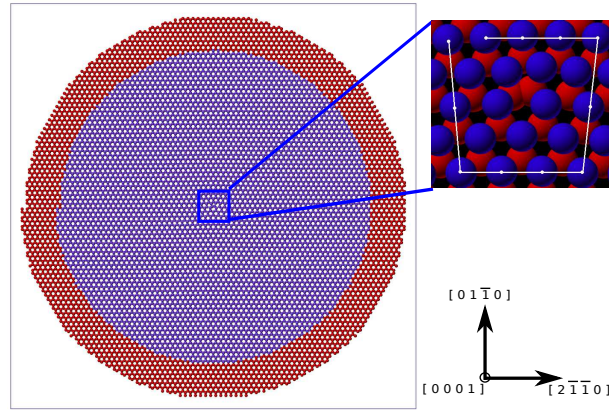
FIG. 3. (Color online) Volterra construction used to create an edge dislocation. The dislocation is at the center of the cell, with its line direction ξ along the [0001] direction. The simulation cell is periodic along ξ. In the close up of the dislocation core, the topmost layer of atoms are colored blue.

atomistics was made. The choice of edge dislocation was made for two reasons: (a) there exists an analytical expression for the strain field, and (b) the strain field itself is complex enough to simultaneously test multiple components of the dipole tensor. Due to the strain field induced by the presence of the edge dislocation, the formation energy of the point defect is modified by an amount ΔE, and can be computed either (a) directly from atomistics, or (b) from equation 1. In this subsection, we describe the steps taken to compute ΔE.

For an edge dislocation in an HCP crystal with Burgers vector $\mathbf{b} = \mathbf{b}_x + \mathbf{b}_y$, the displacement field is given within the purview of anisotropic elasticity[41], and the strain fields are obtained by computing the appropriate derivatives of the displacement field. Note that the expressions for the displacement field are valid only if either (a) the dislocation line is an axis of sixfold symmetry or (b) every axis is an axis of evenfold symmetry. A dislocation with Burgers vector $\mathbf{b} = \frac{1}{3}[2\bar{1}\bar{1}0]$ on the $(01\bar{1}0)$ slip plane was chosen, as it satisfies the first condition, i.e., the Z axis is one of sixfold symmetry. It is possible to construct a dislocation with the same Burgers vector on the (0001) slip plane, but we observed that on the (0001) slip plane, the edge dislocation dissociates into Shockley partials with mixed character.

The atomistic model of the edge dislocation was created using a Volterra construction as follows: the starting point was a perfect crystal in the shape of a cylinder, of radius ≈ 100Å, and height ≈ 20Å. The cylinder was centered at the origin of the simulation box, with its axis along the Z direction. The box itself was periodic in the Z direction, and large enough to accommodate the cylinder along the X and Y directions. All atoms of this cylinder were displaced according to the displacement field computed using anisotropic elasticity theory. The "skin" atoms (atoms within twice the cutoff distance of the EAM potential from the periphery of the cylinder) were frozen, while the interior atoms were allowed to relax. The top view of the relaxed structure, with the skin atoms colored red, is shown in Fig. 3. Here, the dislocation is located at the origin, which is the center of the cell, and the dislocation line ξ is perpendicular to the plane of viewing. The value of ΔE for the vacancy was computed at various spatial locations by deleting a single atom, relaxing the structure, and computing the relative vacancy formation energy, using a vacancy in a strain free environment as the reference.

Figure 4 shows a plot of ΔE computed using both atomistics and equation 1 using the strain tensor obtained from elasticity theory, as a function of distance from the dislocation core, for a few selected angles (as per convention, the angle θ increases in the counterclockwise direction in the XY plane). Results are in good agreement, except near the core, as expected. This is due to the breakdown of elasticity theory, which is known to be invalid near the core of a dislocation, and not a limitation of the dipole tensor approach. It is expected that with a properly computed strain field (using methods such as Falk and Langer's method[42] of using a least squares fit to the displacement to compute the deformation gradient, the Voronoi polyhedra approach of Mott et al.[43], or the least squares method used by Shenogin and Ozisik[44,45]), the agreement of atomistics with the predicted values will be better.

C. Vacancy dynamics

The dynamics of a vacancy were validated by computing its diffusivity, using both MD and kMC, in strained and unstrained environments. Diffusivity along each coordinate direction was computed using a least squares fit to the linear portion of the mean square distance as a function of time[46] as:
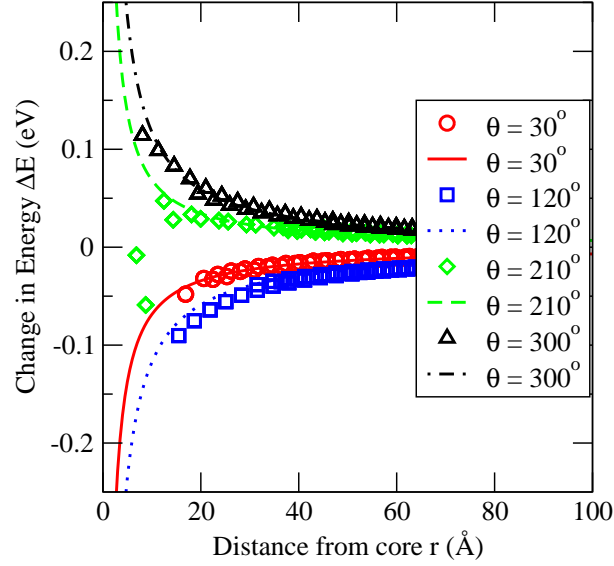
FIG. 4. (Color online) Change in vacancy energy, ΔE, as a function of position in the vicinity of the edge dislocation prepared using a Volterra construction (shown in Fig. 3). As per convention, θ increases in the counterclockwise direction in the XY plane. Points are data obtained from atomistics, while lines are obtained using the dot product of the dipole tensor $\mathbf{G}$ and the strain tensor ε (obtained using anisotropic elasticity theory). Predicted values begin to deviate from atomistic values at $r < 20\text{Å}$.

$$\langle R_i^2 \rangle = 2D_i t \quad ; \quad i \in [x, y, z] \tag{7}$$

where the average was computed over more than 3500 independent trajectories. The strain tensor imposed was of the form

$$\varepsilon = \begin{pmatrix} \varepsilon_0 & 0 & 0 \\ 0 & -\varepsilon_0 & 0 \\ 0 & 0 & 0 \end{pmatrix} \quad ; \quad \varepsilon_0 \geq 0 \tag{8}$$

corresponding to tensile strain along the X direction, and compressive along the Y direction. Since the dipole tensor components presented in table I are relatively small, it was found necessary to use values of the parameter $\varepsilon_0 \geq 0.02$ to observe measurable effects. Fig. 5 shows the diffusivity as a function of the parameter ε_0. The MD results agree well with the kMC results, until anharmonicity effects start to become important (seen in the MD data at the highest temperatures). For the unstrained case, diffusion is isotropic in the basal plane, i.e. $D_x = D_y$ as expected, but there is anisotropy between the X and Z directions because of the symmetry of HCP materials. For the strained case, the asymmetric strain in the X and Y directions breaks the symmetry of the basal plane, resulting in fully anisotropic diffusivity with $D_x \neq D_y \neq D_z$. Also, compared with the unstrained state, diffusivity in all three directions is enhanced. This is because compressive strain in the Y direction increases the rate of transitions that have X and Z components as part of their displacement vector. These results show that the kMC catalog is complete, the dipole tensor approach predicts the change in energy barriers accurately, and that Gillan's strain derivative relationship for computing the dipole tensor are valid for both the minimum and the saddle point of a transition.

D. Limitations

While results presented in the preceding sections demonstrate that the dipole tensor approach is capable of accurately accounting for arbitrary strain fields, it is important to discuss some of the limitations of this approach. The main assumption of this approach is that the elastic response of the environment of the defect is well approximated by that of perfect bulk. In its present form, this technique should not be applied to defects at or near free surfaces or
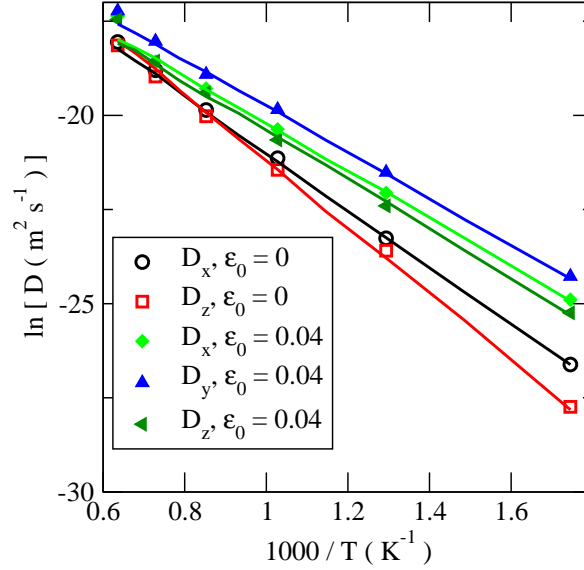
FIG. 5. (Color online) Diffusivity of single vacancy shown on an Arrhenius plot for $\varepsilon_0 = 0$ (strain free), and $\varepsilon_0 = 0.04$ ($\varepsilon_{xx} = 0.04, \varepsilon_{yy} = -0.04$). In the absence of strain, diffusion in the basal plane is isotropic, and thus, D_y for this case is not shown. Points are results from MD, and lines are results from kMC.

interfaces. However, if an appropriate surrogate for the bulk behavior is identified, the concepts discussed here can be directly translated.

Another important assumption is that the fundamental structure of the kMC catalog is unchanged by the introduction of strain. This is a result of assuming that the underlying topology of the potential energy surface is independent of strain: while strain might change the energy of minima, the connectivity graph between them is unchanged, and the strain serves only to change the relative heights of stationary points on the surface.

Preliminary results obtained for self interstitial atoms (SIAs), presented in Fig. 6, demonstrate a first scenario that violates our assumptions: as a crystal with a single SIA is strained, at $\varepsilon_{xx} \approx 0.008$, the saddle between the basal octahedral (BO) structure of a SIA, and the basal crowdion (BC) structure disappears, and the BO structure spontaneously transforms into a BC. Note that this result is a function of the potential, and what happens in real zirconium might be different, a possibility that can be explored using density functional theory. Nevertheless, this example illustrates one of the hazards of using the dipole tensor approach to inform a kMC catalog, and thus while running a simulation, it is important to periodically check if the topology of the potential energy surface has been modified. The dipole tensor approach itself provides a cheap on the fly check to identify some scenarios: in Fig. 6, the red broken line is the barrier for transformation as a function of strain, as predicted by the dipole tensor. The horizontal black broken line indicates $E_a = 0$. For the BO $\rightarrow$ BC transformation, the energy barrier computed using the dipole tensor approach becomes negative at $\varepsilon_{xx} \approx 0.005$, suggesting that the rate catalog is no longer physical.

The reverse scenario is also possible: states that were not energy minima in the absence of strain turn into energy minima when a strain is applied. This latter scenario is illustrated schematically in Fig. 7, and poses a more serious problem: computation of a zero strain kMC catalog would not reveal the existence of a hitherto unknown minimum which could change the connectivity of the catalog, and possibly have profound implications for the dynamics. In such a situation, it might be useful to choose the strained state as the reference from which dipole tensors are computed.

Note that some of these limitations can be partially addressed by computing dipole tensors around multiple reference strain states. However, even in its simple form, the dipole tensor approach allows for incorporation of the effects of strain that affect defect mobility, and will yield much more physical and accurate results than if the strain effects are not accounted for. This is illustrated in the next section.
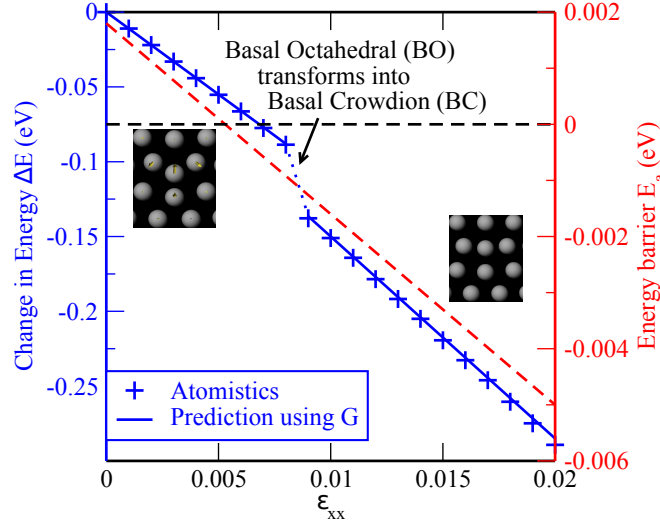
FIG. 6. (Color online) Spontaneous transformation of a SIA under strain: results of straining a Basal Octahedral (BO) SIA structure. Points are data obtained using atomistics. At $\varepsilon \approx 0.008$, the BO structure spontaneously transforms into a Basal Crowdion (BC). Straight blue lines are predictions to ΔE using the dipole tensor of the respective structure. Insets show a view of both structures looking down the c axis. Arrows on the atoms in the BO structure (upper left) show the displacement of atoms in going to BC. The broken inclined red line shows the energy barrier for the transformation, as predicted using the dipole tensor, and the horizontal broken line marks $E_a = 0$.
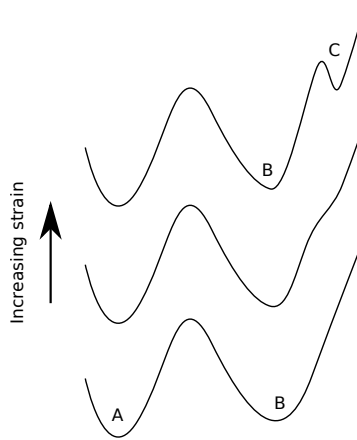

FIG. 7. A possible scenario that violates the fundamental assumption used in the dipole tensor approach. As strain increases, the original energy landscape (bottom curve) changes and acquires a new minimum C, and corresponding transitions that were nonexistent in the unstrained case into the rate catalog.

IV. APPLICATIONS

Some rate theory calculations done in the past assume for simplicity (see e.g. work by Stoller et al.[47] or Rottler et al.[48]) that the point defect absorption rate of sinks, such as dislocations, is spatially homogeneous, with the spatial heterogeneity being subsumed into model parameters. Using the methodology outlined and validated above, it is now possible to compute more accurate values of point defect absorption rates by sinks without resorting to parameters. Furthermore, it is also possible to accurately compute the partitioning of point defect fluxes into different sinks which have different and potentially interacting strain fields as a function of the spatial distribution of sinks. In this section, a few demonstrations of the capability outlined above are presented.
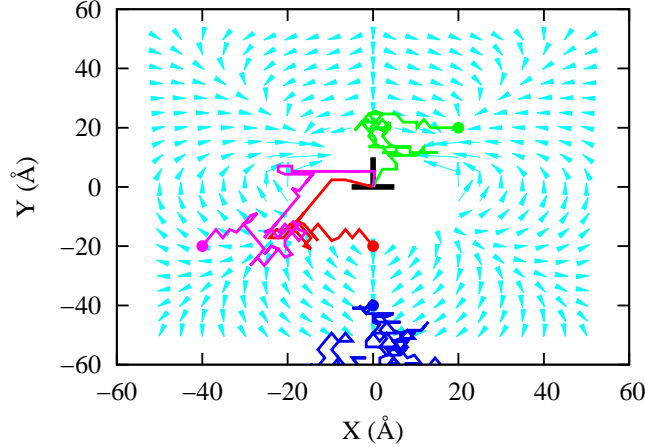
FIG. 8. (Color online) The vector **w**, computed as the rate weighted average displacement, as a function of position, in the vicinity of an edge dislocation. Only a two dimensional slice at $Z = 0$ is shown. The vector **w** shows the most likely direction of motion of the vacancy. Also shown are 2D projections of a few representative trajectories of the vacancy. Solid circles show the starting point of the trajectory.

A. Strain induced vacancy migration inhomogeneity

The edge dislocation described in the previous sections was used as the test sink, and the mobility of a vacancy in its field was examined. At various points in the vicinity of the edge dislocation, the rates of each possible transition, $k^{(i)}$, were computed at 500 K, and the rate weighted average displacement vector, **w**, was computed at each point as

$$\mathbf{w} = \frac{\sum_i k^{(i)} \mathrm{d}\mathbf{r}^{(i)}}{\sum_i k^{(i)}} \tag{9}$$

where the summation is over all possible transitions for a vacancy (six in plane and six out of plane), over two types of vacancies (A plane and B plane) for a total of 24 possible transition. The vector **w** is thus an indicator of the vacancy flux in the vicinity of the edge dislocation. A value of $|\mathbf{w}| = 0$ indicates that the vacancy executes a hop in a random direction at that position: all directions are equally probable. A non zero value, on the other hand, indicates that the vacancy is on average predisposed towards executing a step in the direction of **w**, and the magnitude of the bias is proportional to the magnitude of **w**. The results of this computation are shown as a vector plot in Fig. 8, which is a two dimensional slice at $Z = 0$. The bias in vacancy mobility introduced by the dislocation is clearly visible. In the lower half of the figure, the repulsive side of the edge dislocation shows flux lines pointing away from the dislocation, while the opposite attractive side shows flux lines pointing towards the dislocation. The flux lines also circle from the repulsive side to the attractive side, indicating that a vacancy placed on the repulsive side has a tendency to make its way over to the attractive side before being absorbed: a characteristic of the flux lines predicted from continuum elasticity theories. Far away from the dislocation, the vacancy sees little or no bias in its mobility. As it approaches the dislocation, the bias becomes more pronounced.

Superimposed on this plot are two dimensional projections of a few sample vacancy trajectories. The starting point of each trajectory is shown by a solid circle, and the trajectories behave in accordance with the bias introduced by the dislocation. The red and blue trajectories begin in initially repulsive regions. The red trajectory moves to an attractive region before it gets absorbed into the dislocation. The blue trajectory, on the other hand, never makes it to the attractive side and escapes. The green and purple trajectories start in attractive sides of the dislocation and get absorbed. Note that these trajectories are just indicators of typical behavior, and depending on the temperature, some trajectories might behave differently.

B. Vacancy absorption rate in the vicinity of an edge dislocation

In this second test, a vacancy was placed at a given point (x, y) (grid points in Fig. 9) in the vicinity of the dislocation. The system was evolved using the kMC algorithm described in section II C in a cubic simulation box of side 1×10^5 Å at 500 K (typical cladding temperature for an operational reactor). If the vacancy reached the interior of
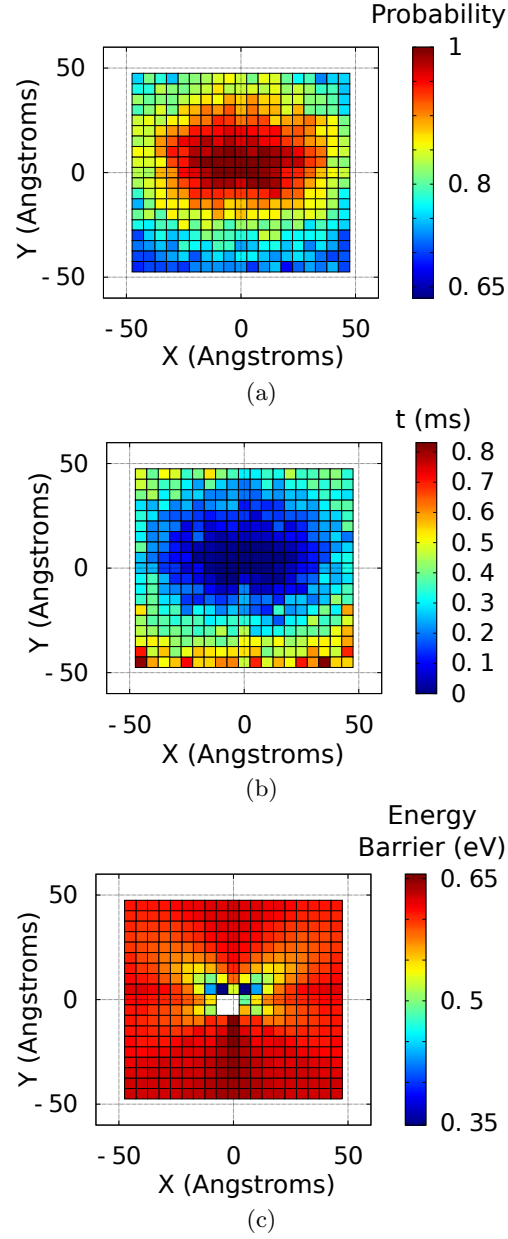
FIG. 9. (Color online) In the vicinity of the dislocation described in section III B, (a) probability of absorption by the dislocation, (b) mean lifetime if absorbed, and (c) lowest barrier for a vacancy hop. The dislocation is located at the origin, with its line direction ξ along the Z axis. The spatial inhomogeneity due to the strain field is reflected in all three figures.

a cylinder of radius 3 Å surrounding the dislocation, it was considered absorbed, a counter was incremented, and the time taken by the vacancy to be absorbed was noted. If, on the other hand, the vacancy reached the edge of the box, it was considered to have escaped. This process was repeated over 700 times for each point (x, y), and the probability of absorption (P), and the mean time to absorption (t) were computed. The process was repeated at multiple spatial locations, and the two quantities P and t as a function of position are shown in Fig. 9 (a) and (b). The lowest barrier as a function of position is shown in Fig. 9 (c), indicating the spatial variation of the barrier associated with the most probable event. In these simulations, the edge dislocation is located at the origin, with its line direction ξ along the Z axis. We see that the asymmetry is a consequence of the strain field, that leads to variability in absorption times.

C. Vacancy absorption in a periodic array of dislocations

One of the important quantities that is often encountered in defect reaction rate theories[49] is the defect absorption rate A, which directly controls the macroscopic strain rate of the material. Traditionally, the defect absorption rate is computed as

$$A = Dck^2 \tag{10}$$

where D is the defect diffusivity in a strain free bulk environment, c is the defect concentration, and k^2 is a parameter known as sink strength. With the underlying assumption that the mean distance between sinks is significantly less than the mean distance between defects[49], the sink strength is computed using a single defect in a simulation box as follows[50,51]: in a simulation box with periodic boundary conditions, with a microstructure composed of typically only one class of sink, a single defect is introduced at a random position, and followed until it gets absorbed into the sink. Upon absorption, a new defect is introduced, and the procedure repeated. The sink strength is then computed as

$$k^2 = \frac{2n}{d_j^2 \langle n_j \rangle} \tag{11}$$

where d_j is the average distance per jump, $\langle n_j \rangle$ is the average number of jumps executed by the defect before it is absorbed, and n is the dimensionality of the diffusivity D used in equation 10.

This approach suffers from two limitations: (a) it uses the homogeneous bulk diffusivity, which implies a decoupling between diffusion and elasticity, and consequently, contains no information about the spatial inhomogeneity introduced by the sink; and (b) there is no information about the diffusion anisotropy of the defect, which is important for materials like zirconium, i.e., this approach assumes that all hops are equivalent, and thus a simple counting of steps is appropriate. In this subsection, the *quantitative* differences between vacancy absorption rates, computed with and without strain field, are highlighted for two different sink densities, and a range of temperatures.

In a cubic simulation box with periodic boundary conditions (note that the boundary conditions for this simulation box are different from those used in subsection IV A), the edge dislocation described in previous sections was placed at the origin, with its line direction ξ parallel to the Z direction. In addition to the strain field of the dislocation in the simulation box, the strain field of the eight first nearest neighbors was superimposed to obtain the final strain field. By tracking the time to absorption of vacancies (a vacancy was considered absorbed if it reached the interior of a cylinder of radius 3 Å surrounding the dislocation) placed one by one in the field of the edge dislocation, as in section IV A, the absorption rate A was computed as the reciprocal of the spatially averaged mean time to absorption. This way of computing A removes any ambiguity associated with choosing a value for the diffusivity D, which can be a difficult choice, particularly for anisotropic materials such as zirconium.

Figure 10 shows a plot of the ratio of the quantity $A(\varepsilon)/A(\varepsilon = 0)$, which is the ratio of absorption rates computed in the presence, and absence of dislocation strain fields, for two different dislocation densities of $\rho = 10^{15}$ m^{-2}, and $\rho = 10^{16}$ m^{-2}, which correspond to realistic dislocation densities of cold worked material. The results show that as the temperature approaches zero, the ratio increases, and we expect it to plateau as $T \rightarrow 0$. This is because at lower temperatures, the strain induced bias in vacancy mobility is more pronounced, and vacancies have a more direct path to the dislocation. If a vacancy starts on the repulsive side of a dislocation, it migrates until it crosses the periodic boundary, makes it to the attractive side of the dislocation, and gets absorbed in a relatively small number of steps. This results in an enhancement of the absorption rate. On the other hand, vacancies in the absence of strain have to perform a random walk, the length of which is on average unchanging with temperature, to get to the dislocation. At high temperatures, the effects of strain become less important: the vacancy trajectory is more random even in the presence of strain, and the ratio asymptotes to unity. Strain effects are less pronounced for the lower dislocation density, as the strained region is a smaller fraction of the simulation box. This strain induced enhancement of absorption rate is a factor between 2 and 4 for normal reactor operating temperatures of ≈ 500 K, and can reach factors in excess of 30, for temperature and dislocation densities that might be more relevant for laboratory conditions. It is also important to note that we do not expect this demonstration to change qualitatively as the interatomic potential is changed: any reasonable potential for zirconium is expected to capture the in plane and out of plane transitions, as well as the energy changes as a function of strain. Thus, this demonstration might be considered semi independent of the potential, and that the phenomenon of strain induced absorption rate enhancement is a universal feature in all materials.
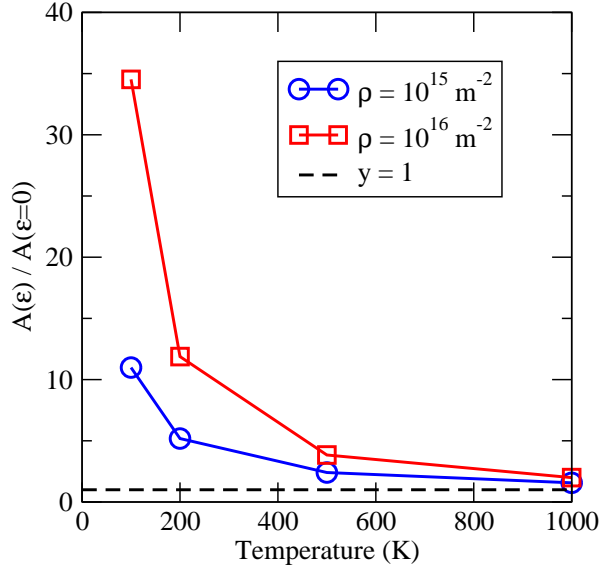
FIG. 10. (Color online) Ratio of absorption rates A computed with and without the effect of strain fields for dislocation densities representative of cold worked material. Strain effects become less important at higher temperatures, and lower dislocation densities.

D. Possibilities for future enhancements and applications

In the above examples, only one defect was simulated in any given realization of the system. Interactions between point defects have not been taken into account, but can easily be incorporated into the kMC framework presented above. Other subjects of interest that can be incorporated with relative simplicity into the framework include the presence of multiple types of sinks (such as screw dislocations, loops, voids, and even a complex tangle of dislocations that may be predicted from dislocation dynamics simulations), partitioning of point defect flux into different sinks, and evolution of the sinks themselves.

The input strain field required for these complex scenarios is generally not available in closed form. In such situations, the strains can be calculated atomistically (using either the least squares approach to computing the deformation gradient[42], or the Voronoi polyhedra approach[43]) and used as input into the simulation, and the atomistic strain fields can be updated anytime the defect becomes part of the sink. The strain fields required in such situations are the strain fields in the absence of the defects, and it is assumed that the defect is in an environment that is well approximated by the bulk.

These examples are a small subset of the possible extensions to the scheme presented in this work, and will be explored in detail in future publications.

V. CONCLUSIONS

A scheme that accounts for the influence of arbitrary strains on defect transition rates in kinetic Monte Carlo was outlined. This scheme uses the dipole tensor to rapidly compute strain induced changes in transition rates, and requires the inexpensive computation of the double dot product of two tensors, as opposed to recomputing the rate catalog from scratch, or even reconverging saddles in the presence of strain.

This scheme can only compute the changes in rates for predefined events, and while running an actual simulation, it would be advisable to periodically check to see if any of the assumptions underlying the scheme have been violated. The benefits of using this scheme far outweigh the limitations, the latter of which can be guarded against, if not on the fly, at least after the fact, to improve the quality of the simulation.

The power of this scheme is that quantities such as point defect absorption rates, which naturally depend on sink distributions, can be more directly calculated, accounting for all variations in strain fields in the material, with a significant savings in computational effort. This scheme allows more accurate computation of parameters, such as sink strength and sink efficiency, that are used in traditional irradiation damage models. Accurate computations of point defect absorption rates are critical for predicting mesoscale phenomena, such as dislocation climb and loop
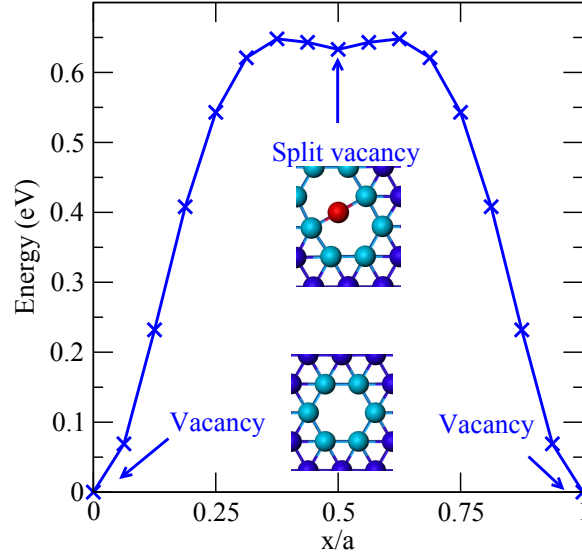
FIG. 11. (Color online) Energy as a function of reaction coordinate for vacancy migration in the basal plane. The reaction coordinate is given by the distance moved by the vacancy, x, normalized by the lattice parameter, a.

growth, which determine microstructural evolution under irradiation. The scheme itself can be extended to any system where strain influences mobility. This approach could also be incorporated in an adaptive kMC, where saddles are computed on the fly, and barriers are updated via the dipole tensor.

For the application of this scheme to more complex defects, such as interstitial clusters or voids, computing the rate catalog of the complex defect is a real and challenging problem as the number of transitions associated with a complex defect can be astronomical. As stated in the introduction, the exploration of the potential energy landscape can be a formidable challenge, and is an issue for all kMC simulations. One way of dealing with complex defects, within the framework outlined in this paper, is to obtain an effective energy barrier from an Arrhenius plot of diffusivity vs. temperature at various strains, and compute an effective dipole tensor for the complex defect. This is more akin to traditional OKMC simulations in which objects are treated in an average sense, rather than accounting for every atomic process that describes their motion. This simplistic approach might not be straightforward to put into practice because of some interesting features presented by complex defects that warrant further investigation, such as (a) crowdion clusters in zirconium are known to be rapid one dimensional diffusers[52], and (b) there exist magic sized islands that exhibit non Arrhenius behavior[53]. Addressing these interesting features posed by complex defects remains an open question, and we hope to address these issues in future publications.

VI. ACKNOWLEDGMENT

Appendix A: Split vacancy

Fig. 11 shows the energy along the reaction coordinate for a vacancy hopping from one lattice site to the next within the basal plane. Here, the reaction coordinate, x/a, is the distance moved by the vacancy, x, normalized by the lattice parameter, a. Also shown are snapshots of the basal plane containing the vacancy, and the intermediate split vacancy configuration. The barriers for the transformations are $E_a(\text{normal} \rightarrow \text{split}) = 0.654\text{eV}$, and $E_a(\text{split} \rightarrow \text{normal}) = 0.010\text{eV}$. The only two minima that the split vacancy was observed to be capable of transforming into were two normal vacancies, corresponding to $x/a = 0$ and $x/a = 1$. For temperatures in the range $T \in [300 : 900]$,

the ratio of $E_a(\text{split} \rightarrow \text{normal})/k_B T$ is in the range of $[0.39 : 0.13]$, and can therefore be ignored.

This claim was substantiated by observing MD trajectories of a vacancy in the following manner: the starting point was a minimized configuration of a single vacancy in the normal vacancy position. The system was thermalized to 973K, and the equations of motion were integrated, quenching the trajectory every 5 fs, and comparing the resulting configuration with the starting configuration, until the vacancy made its first hop. If the hop was out of the basal plane, the trajectory was discarded, and the process was started again with a different random number seed. If, however, the hop was in the basal plane to the split vacancy structure, the trajectory was continued until the second hop was made. If the second hop was in the direction opposite the first hop, a "backward" counter was incremented. This counter kept track of how many times a vacancy hopped back to its original position after transforming into a split vacancy. If the second hop was in the same direction as the first hop, a "forward" counter was incremented. After two hops, the original starting configuration was restored, and the process was repeated with a different random seed. Upon repeating this experiment 137 times, it was found that the number of times a split vacancy jumped back into its original position was 3, and the mean lifetime of a split vacancy was 0.3 ps. This implies that the majority (over 97%) of transitions from a vacancy to a split vacancy continue on, with the net effect of moving the vacancy by a lattice constant, and thus, the split vacancy as an explicit minimum can be neglected.

Appendix B: The full kMC catalog for a vacancy

The full kMC catalog for a vacancy is obtained by performing symmetry operations on the minimum, and the two basic transitions associated with the minimum. The two basic transitions of a vacancy are (a) the in plane hop along the X direction, and (b) the out of plane hop with a zero X component, as outlined in table I. Each type of transition has different sets of symmetry operations. For the in plane transition, the first two symmetry equivalents are obtained by performing $120°$ and $240°$ rotations about the Z axis. The resulting set of three transitions are reflected across the YZ plane to obtain the set of six in plane transitions. For the out of plane transitions, the first two rotational symmetry operations remain the same, but the reflection is performed across the XY plane. These symmetry operations can be characterized by the following transformation matrices: for the in plane transition, the matrices are

$$\mathbf{R}_{ip} = \begin{bmatrix} p & 0 & 0 \\ 0 & 1 & 0 \\ 0 & 0 & 1 \end{bmatrix} \begin{bmatrix} \cos(n\theta) & -\sin(n\theta) & 0 \\ \sin(n\theta) & \cos(n\theta) & 0 \\ 0 & 0 & 1 \end{bmatrix} \tag{B1}$$

while the matrices for the out of plane transition are

$$\mathbf{R}_{oop} = \begin{bmatrix} 1 & 0 & 0 \\ 0 & 1 & 0 \\ 0 & 0 & p \end{bmatrix} \begin{bmatrix} \cos(n\theta) & -\sin(n\theta) & 0 \\ \sin(n\theta) & \cos(n\theta) & 0 \\ 0 & 0 & 1 \end{bmatrix} \tag{B2}$$

Here, n is an integer in the range $[0, 5]$, $\theta = 120°$, $p = 1$ if $n \leq 2$, and $p = -1$ if $n > 2$, and we have exploited the fact that a rotation by θ is equivalent to a rotation by $360° + \theta$.

Furthermore, due to the $ABAB$ stacking sequence of HCP, the transitions associated with an A plane vacancy are different from those of a B plane vacancy. Thus, the vacancy state, and the 12 transitions obtained in the previous step were rotated about the Z axis by $180°$ to obtain a second state with its own set of 12 transitions. The kMC catalog also contained the information that an in plane transition did not change the character of the vacancy, while an out of plane transition changed a vacancy from A type to B type, and vice versa.

Another complication was posed by the asymmetry of the in plane transition. If the split vacancy is ignored as a state, there are two saddle points that a vacancy has to pass over when executing a hop. In Fig. 11, one saddle point is at $x/a \approx 0.375$, and the other at $x/a \approx 0.625$. These two saddle points are asymmetric with respect to shear strain, i.e., the application of a shear strain raises one of these saddles, and lowers the other. Thus in the kMC simulations, when the saddle point energies were calculated as a function of strain, both saddles were accounted for, and the higher of the two saddles was taken to be the relevant one for the in plane transition. Note that this extra step needs to be incorporated into the kMC algorithm, so that the same saddle point is picked for both the forward and backward transitions. Furthermore, in the kMC procedure, the strain at the mid point of the transition is taken to be the strain at the saddle point. This was done for simplicity, and in general, the saddle point of the transition is not necessarily at the mid point of the transition.

* gss@lanl.gov

1 A. Bortz, M. Kalos, and J. Lebowitz, Journal of Computational Physics, **17**, 10 (1975), ISSN 0021-9991.
2 A. F. Voter, in *Radiation Effects in Solids*, NATO Science Series, Vol. 235, edited by K. E. Sickafus, E. A. Kotomin, and B. P. Uberuaga (Springer Netherlands, 2007) pp. 1–23, ISBN 978-1-4020-5295-8.
3 J. Deppe, R. F. Wallis, I. Nachev, and M. Balkanski, Journal of Physics and Chemistry of Solids, **55**, 759 (1994).
4 Q. Xu and A. Van der Ven, Physical Review B, **81** (2010), ISSN 1098-0121, doi:10.1103/PhysRevB.81.064303.
5 D. Das, D. Das, and A. Prasad, Journal of Theoretical Biology, **308**, 96 (2012), ISSN 0022-5193.
6 G. Martin, F. Soisson, and P. Bellon, Journal of Nuclear Materials, **205**, 301 (1993).
7 H. Xu, Y. N. Osetsky, and R. E. Stoller, Journal of Nuclear Materials, **423**, 102 (2012), ISSN 0022-3115.
8 R. W. Smith, Journal of Applied Physics, **81**, 1196 (1997).
9 E. Antoshchenkova, M. Hayoun, F. Finocchi, and G. Geneste, Surface Science, **606**, 605 (2012), ISSN 0039-6028.
10 M. A. Novotny, Phys. Rev. Lett., **74**, 1 (1995); Erratum, *ibid.*, **75**, 1424 (1995).
11 G. Henkelman and H. Jónsson, The Journal of Chemical Physics, **115**, 9657 (2001).
12 C. Domain, C. Becquart, and L. Malerba, Journal of Nuclear Materials, **335**, 121 (2004), ISSN 0022-3115.
13 A. Chatterjee and A. F. Voter, The Journal of Chemical Physics, **132**, 194101 (2010).
14 G. H. Vineyard, Journal of Physics and Chemistry of Solids, **3**, 121 (1957), ISSN 0022-3697.
15 B. C. Bolding and E. A. Carter, Surface Science, **268**, 142 (1992), ISSN 0039-6028.
16 P. Meakin and K. M. Rosso, The Journal of Chemical Physics, **129**, 204106 (2008).
17 W. Guo, T. P. Schulze, and W. E, Communications in Computational Physics, **2**, 164 (2006).
18 C. Ratsch, Phys. Rev. B, **83**, 153406 (2011).
19 M. Hane, T. Ikezawa, and A. Furukawa, IEICE Transactions on Electronics, **E83-C**, 1247 (2000).
20 E. Pastukhov, A. Vostrjakov, N. Sidorov, and V. Chentsov, Defect and Diffusion Forum, **279–301**, 193 (2010).
21 E. J. Savino and C. N. Tomé, Journal of Nuclear Materials, **108**, 405 (1982), ISSN 0022-3115.
22 M. Kaukonen, J. Peräjoki, R. M. Nieminen, G. Jungnickel, and T. Frauenheim, Phys. Rev. B, **61**, 980 (2000).
23 A. Ramasubramaniam, M. Itakura, M. Ortiz, and E. Carter, Journal of Materials Research, **23**, 2757 (2008).
24 Z. Chen, N. Kioussis, N. Ghoniem, and D. Seif, Phys. Rev. B, **81**, 094102 (2010).
25 D. Matsunaka and Y. Shibutani, Journal of Physics: Condensed Matter, **23**, 265008+ (2011), ISSN 0953-8984.
26 N. Castin and L. Malerba, The Journal of Chemical Physics, **132**, 074507 (2010).
27 L. Nurminen, A. Kuronen, and K. Kaski, Phys. Rev. B, **63**, 035407 (2000).
28 T. P. Schulze and P. Smereka, Communications in Computational Physics, **10**, 1089 (2011).
29 M. I. Mendelev and G. J. Ackland, Philosophical Magazine Letters, **87**, 349 (2007).
30 H. Jónsson, G. Mills, and K. W. Jacobsen, in *Classical and Quantum Dynamics in Condensed Phase Simulations*, edited by B. J. Berne, G. Ciccotti, and D. F. Coker (World Scientific, 1998) p. 385.
31 G. Henkelman and H. Jónsson, Journal of Chemical Physics, **113**, 9978 (2000).
32 G. Henkelman, B. P. Uberuaga, and H. Jónsson, The Journal of Chemical Physics, **113**, 9901 (2000).
33 E. Kröner, *Kontinuumstheorie der Versetzungen und Eigenspannungen* (Springer-Verlag, Berlin, 1958).
34 A. S. Nowick and B. S. Berry, *Anelastic Relaxation in Crystalline Solids* (Academic Press, New York, 1972).
35 G. Leibfried and N. Breuer, *Point Defects in Metals*, Vol. 1 (Springer-Verlag, Berlin, 1978).
36 H. Kanzaki, Journal of Physics and Chemistry of Solids, **2**, 24 (1957).
37 J. R. Hardy and A. B. Lidiard, Philosophical Magazine, **15**, 825 (1967).
38 M. J. Gillan, Philosophical Magazine A, **48**, 903 (1983).
39 M. J. Gillan, Journal of Physics C: Solid State Physics, **17**, 1473 (1984).
40 E. Hayward, C. Deo, B. P. Uberuaga, and C. N. Tomé, Philosophical Magazine, **92**, 2759 (2012).
41 J. P. Hirth and J. Lothe, 2nd ed. (Krieger Publishing Company, Malabar, Florida, 1992).
42 M. L. Falk and J. S. Langer, Physical Review E, **57**, 7192 (1998).
43 P. H. Mott, A. S. Argon, and U. W. Suter, Journal of Computational Physics, **101**, 140 (1992), ISSN 0021-9991.
44 S. Shenogin and R. Ozisik, Polymer, **46**, 4397 (2005), ISSN 00323861.
45 S. Shenogin and R. Ozisik, Journal of Polymer Science Part B: Polymer Physics, **43**, 994 (2005), ISSN 1099-0488.
46 A. Einstein, *Investigations on the Theory of the Brownian Movement* (Dover publications, 1956).
47 R. Stoller, S. Golubov, C. Domain, and C. Becquart, Journal of Nuclear Materials, **382**, 77 (2008).
48 J. Rottler, D. J. Srolovitz, and R. Car, Phys. Rev. B, **71**, 064109 (2005).
49 G. S. Was, *Fundamentals of Radiation Materials Science* (Springer-Verlag, 2007).
50 H. L. Heinisch and B. N. Singh, Philosophical Magazine, **83**, 3661 (2003).
51 L. Malerba, C. S. Becquart, and C. Domain, Journal of Nuclear Materials, **360**, 159 (2007).
52 N. Dediego, Y. Osetsky, and D. Bacon, Journal of Nuclear Materials, **374**, 87 (2008).
53 O. U. Uche, D. Perez, A. F. Voter, and J. C. Hamilton, Phys. Rev. Lett., **103**, 046101 (2009).